Wearable Non-Invasive Arterial Pulse Detection with a Millimeter-wave Radar

Nima Bahmani
nima.bahmani@aalto.fi
Aalto University
Espoo, Finland

Dariush Salami
dariush.salami@aalto.fi
Aalto University
Espoo, Finland

Huseyin Yigitler
yusein.ali@aalto.fi
Aalto University
Espoo, Finland

Juhapekka Hietala
juhapekka.hietala@aalto.fi
Aalto University
Espoo, Finland

Tuukka Panula
tuukka.j.panula@utu.fi
University of Turku
Turku, Finland

Stephan Sigg
stephan.sigg@aalto.fi
Aalto University
Espoo, Finland

Abstract

Cardiovascular diseases remain a leading cause of mortality and disability. The convenient measurement of cardiovascular health using wearables is a key enabler to foster continuous, accurate and early detection, diagnosis and management of cardiovascular diseases. We integrate Photoplethysmography (PPG) and mmWave sensing in a mobile wearable device to detect the Inter-beat interval (IBI) and arterial pulse wave. Particularly, We have developed a hardware prototype that integrates both sensing modalities and have verified the system against the gold clinical standard reference with a diverse population of 23 subjects.

CCS Concepts

• **Human-centered computing** → **Ubiquitous and mobile computing systems and tools**; **Empirical studies in ubiquitous and mobile computing**; • **Applied computing** → **Consumer health**; *Health informatics*.

Keywords

Wearable computing, Mobile smart systems, Arterial pulse wave, mmWave, PPG

ACM Reference Format:

Nima Bahmani, Dariush Salami, Huseyin Yigitler, Juhapekka Hietala, Tuukka Panula, and Stephan Sigg. 2025. Wearable Non-Invasive Arterial Pulse Detection with a Millimeter-wave Radar. In *Proceedings of the 2025 ACM International Symposium on Wearable Computers (ISWC '25), October 12–16, 2025, Espoo, Finland*. ACM, New York, NY, USA, 7 pages. https://doi.org/10.1145/3715071.3750411

1 Introduction

Blood pressure, a fundamental physiological parameter, serves as a crucial indicator of the cardiovascular system's function and is a key vital sign monitored in clinical settings [30, 36]. Its accurate and continuous assessment is important for the early detection, diagnosis, and management of cardiovascular diseases, which is still one of the most important cause of disability [27, 38]. Traditional methods of blood pressure monitoring, often relying on intermittent cuff-based measurements, have limitations to provide continuous blood pressure fluctuations and can be inconvenient for routine or overnight monitoring [30, 31, 36].

Arterial stiffness, a measure of the elasticity of arterial walls, is increasingly recognized as a significant factor in cardiovascular health [9, 13]. Changes in arterial stiffness are associated with aging, hypertension, and various other cardiovascular disorders, influencing the morphology of the arterial pulse wave [13, 38]. These functional alterations in the pulse wave contour impose an increased workload on the cardiovascular system, thereby emphasizing why accurate characterization of arterial pulse wave is necessary for a robust cardiovascular evaluation [10, 24]. By continuously capturing arterial pulse waveforms and related physiological data, wearable technologies hold significant promise for early detection and more effective management of prevalent conditions such as hypertension and other cardiovascular disorders [19, 21, 38].

IBI, the time between successive heartbeats, offers early indication of emerging cardiovascular conditions [6], carrying valuable information beyond basic heart rate. PPG, one of the most common wearable health sensors [25], provides both a blood volume–based pulse wave and IBI measurements. These are often used to assess heart rate variability, which reflects autonomic nervous system activity and cardiovascular health. PPG is a simple and low-cost optical biosensing solution that supports continuous monitoring [2, 29]. However, for capturing high-fidelity arterial pulse waveforms needed in advanced assessments like arterial stiffness, PPG can face limitations [12, 22].

To address it, combining PPG with a more advanced sensing modality such as mmWave radar in the same device allows side-by-side comparison of their capabilities. PPG enables continuous, energy-efficient monitoring of cardiovascular signals, particularly beat-to-beat timing, while mmWave radar also captures high resolution arterial pulse waveforms at selected intervals. These detailed waveforms can support estimation of arterial stiffness, a biomarker of vascular aging. While there is some overlap, such as in beat timing, their differing strengths, PPG in low-power beat detection and mmWave in morphological detail, motivate their co-location. Together, they form a complementary sensing setup for comprehensive cardiovascular monitoring. To assess signal reliability, we compare both sensing modalities against Continuous Non-invasive Arterial Pressure (CNAP), commonly used as a reference.

ISWC '25, Espoo, Finland

ACM ISBN 979-8-4007-1481-8/2025/10
https://doi.org/10.1145/3715071.3750411

Our contributions are two-fold:

(1) We introduce a novel hardware prototype that integrates reflective PPG and near-field mmWave sensing within a single compact wearable form factor, enabling the first simultaneous acquisition of both signals from the same anatomical site.
(2) We conducted a study on 23 healthy participants to evaluate and compare the ability of both sensing modalities to capture IBI and arterial pulse waveforms. This provides insights into how each modality performs in terms of beat timing accuracy and waveform fidelity compared to CNAP.

2 Related Work

Recent advancements in near-field RF sensing have demonstrated the potential for non-invasive biomedical measurements, both in contactless and wearable configurations. mmWave sensing has typically been explored for its potential in contactless applications; for instance, a study by Wang et al. [34] demonstrated the contactless sensing of IBI. Similarly, Shi et al. [30] introduced a contact-free mmWave radar-based system for blood pressure measurement with a focus on motion robustness. Likewise, Tseng et al. [32] explored cuff-less blood pressure measurement using a microwave near-field self-injection-locked wrist pulse sensor. In addition, Ha et al. [14] demonstrated contactless reconstruction of seismocardiogram waveforms using deep-learning-based radar sensing, highlighting the potential of mmWave for non-wearable, long-range cardiac monitoring.

The present work focuses on a wearable implementation, which supports continuous, on-body monitoring and is well suited for practical, everyday use. Johnson et al. [18, 19] presented a wearable mmWave device designed for the measurement of arterial pulses on the wrist for pulse wave analysis (PWA) and pulse transit time (PTT). Wen et al. [36, 37] also proposed a noninvasive and continuous blood pressure estimation developed by a 120 GHz compact antenna radar, extracting the radar-based pulse transit time (RPTT). Das et al. [11] presented a feasibility study on the non-invasive and continuous measurement of the jugular venous pulse using Frequency Modulated Continuous Wave (FMCW) radar. Li et al. [20] presented a near-field cardiac signal monitor based on radar which can be used as a chest wearing device. Abu-Sardanah et al. [1] utilized mmWave sensing on the chest for cardiorespiratory monitoring. Vysotskaya et al. [33] have demonstrated transformer-based approaches for accurate continuous BP estimation utilizing a 60 GHz radar.

The simultaneous use of RF and PPG can provide complementary information regarding cardiovascular dynamics. PPG and radar sensors can be attached to separate sites on the body. For instance, Ebrahim et al. [26] estimated blood pressure using on-body continuous wave radar in conjunction with PPG under various posture and exercise conditions. The continuous wave radar was implemented on the chest and the PPG was attached into the earlobe of the test participants. Gomes et al. [13], have compared wrist-worn mmWave radar with fingertip PPG and a continuous non-invasive blood pressure (CNIBP) reference device.

Despite growing interest in combining RF and PPG for cardiovascular monitoring, a direct, quantitative comparison of arterial pulse waveforms captured simultaneously by both modalities from the same anatomical location remains largely unexplored.

3 Materials and Methods

The multi-modal prototype was developed in a wristband form factor for data collection, which is illustrated in Fig. 2. The mmWave sensing component of our prototype is based on the Infineon-BGT60TR13C evaluation kit [17]. This radar operates at 60 GHz with more than 5 GHz bandwidth and integrates three receive (RX) and one transmit (TX) antenna [16]. The BGT60TR13C evaluation kit is highly configurable, and its accompanying Software Development Kit (SDK) enables real-time data analysis. We set the frame rate of the radar to 200 Hz. For the optical sensing modality, our prototype incorporates the ams-osram AS7058 analog front end and its extension board [3, 4]. The AS7058 is capable of driving multiple Light Emitting Diodes (LEDs) and reading signals from multiple photodiodes [5]. The extension board connects the optical front end to the AS7058 [4]. We utilize SFH 7072 optical modules, which integrate LEDs of different wavelengths and photodiodes. In the study we primarily utilize the green wavelength from one of the optical modules. A dedicated Printed Circuit Board (PCB) was designed to solder the optical module and route the necessary electrical traces to connect to the AS7058 extension board. The PCB design also includes an opening that properly positions the optical modules for direct contact with the tissue, while ensuring that there is no barrier between the radar antenna and the tissue which is demonstrated in Fig. 2 (D). The enclosure of the prototype positions the mmWave antenna at the desired 3mm distance from the tissue while attaching the optical modules to the skin surface; the rigid enclosure design ensures minimal positional shifts.

As ground truth for validation, we utilize the industry gold standard, CNSystems CNAP consisting of a main display unit, a brachial cuff and a wrist-worn finger cuff unit. The pressure values of the finger cuff are calibrated to brachial BP by the system firmware after an arm cuff measurement is performed.

3.1 Radar Signal Modeling

The mmWave sensor transmits FMCW signals which can be represented as [8]:

$$x_T(t) = A_T\, e^{j\left(2\pi f_c t + \pi \frac{B}{T_c} t^2\right)} \tag{1}$$

where t is time, f_c is the carrier frequency of the chirp signal, B is the bandwidth, A_T is the amplitude of the transmitted signal, and T_c is the chirp duration.

This electromagnetic wave travels towards the tissue, interacts with the tissue, and the reflected wave is received by the antenna. The distance to the tissue is computed as $2(d_0 + \Delta d(t))$, where d_0 is the distance from antenna to tissue and $\Delta d(t)$ is the tissue deformation due to arterial pulsation. The received signal can be formulated as:

$$x_R(t) = A_R\, e^{j\left(2\pi f_c (t-t_d) + \pi \frac{B}{T_c} (t-t_d)^2\right)} \tag{2}$$

where A_R is the amplitude of the received signal and t_d is the time delay of the received signal due to round trip. The FMCW system combines the reflected signal with the transmitted signal, and after

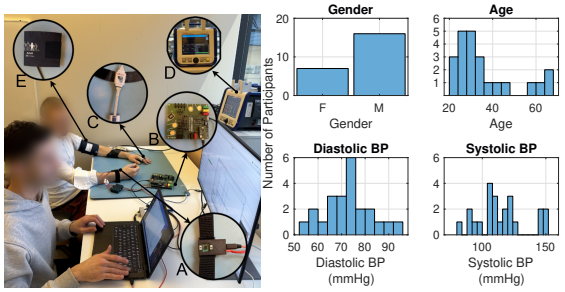

(a) Experiment setup (b) Participant demographics

Figure 1: (a) Setup with (A) Multimodal sensing prototype, (B) ams-OSRAM 7058, (C) CNAP finger cuff, (D) CNAP 500, and (E) Arm cuff. (b) showing the distribution of participant ages and genders, as well as distribution of systolic blood pressure, diastolic blood pressure.

filtering [35], it is converted to an Intermediate Frequency (IF) signal, which can be represented as [30]

$$S_{IF}(t) = x_T(t) \cdot x_R(t) \approx A(t)\, e^{j(2\pi f_d(t) t + \phi(t))},$$
$$A(t) = A_T A_R, \quad f_d(t) = \frac{2B(d_0 + \Delta d(t))}{c \cdot T}, \quad \phi(t) = \frac{4\pi(d_0 + \Delta d(t))}{\lambda}, \tag{3}$$

where $S_{IF}(t)$ is beat signal, and $A(t)$,$f_d(t)$, and $\phi(t)$ are amplitude, frequency and phase of the beat signal, respectively. The arterial pulse waveform in this study is extracted from $\phi(t)$ which is more sensitive to small changes [21].

3.2 Participants

The study involved 23 healthy participants (22 to 65 years, 16 male, 7 female). Fig. 1b shows their baseline systolic and diastolic blood pressure measurements, demonstrating the physiological diversity of the study population.

This diversity was also present in their blood pressure readings, which ranged from 82 mmHg to 151 mmHg for systolic BP, 54 mmHg to 93 mmHg for diastolic BP, and 63 mmHg to 112 mmHg for MAP. This wide range increases the chance of observing a range of pulse wave morphologies, allowing for an evaluation of the multi-modal sensor's ability to track these different patterns accurately.

Participants provided written informed consent prior to enrollment, and the study protocol received approval from the ethics committee of Aalto University (approval ID D/10330/03.04/2024).

3.3 Experimental Setup

We performed experiments in a room with a controlled temperature of 23 degrees Celsius. Participants were seated comfortably in an adjustable-height chair so that their right wrist, where the multimodal sensor prototype was placed, was aligned with heart level. A CNAP Monitor 500 served as gold standard reference for continuous blood pressure measurements. An appropriate arm cuff was fitted to the left arm. After selecting the correct size, finger cuffs were attached to the index and middle fingers of the left hand.

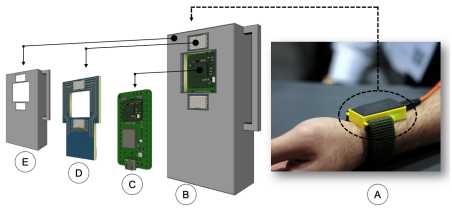

Figure 2: Prototype of the multimodal arterial pulse wave sensing device. (A) The wearable sensor positioned over the radial artery at the wrist. (B) The assembled prototype enclosure housing all sensor components. (C) mmWave radar module for near-field pulse wave sensing, (D) PPG optical front-end, and (E) the protective enclosure featuring a dedicated slot for wrist strap attachment.

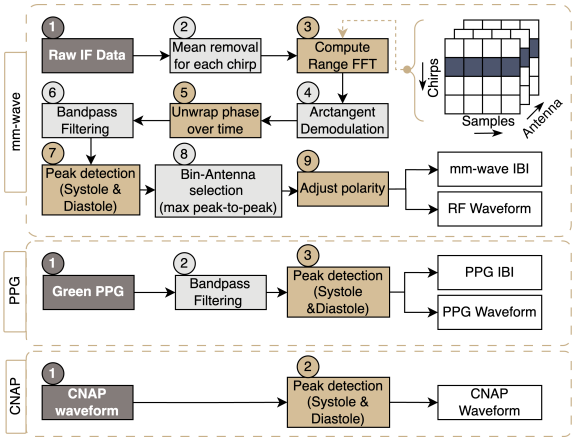

Figure 3: Digital signal processing flowchart.

The CNAP system performed self calibration, and participant physiological information (weight, height, age, gender) was provided to the device.

The multimodal sensor prototype was positioned on the right wrist over the radial artery (located by palpation to maximize signal acquisition). The tightness of the wrist strap securing the prototype was adjusted to ensure consistent skin contact without impeding blood flow. Data from mmWave radar and PPG sensor were acquired simultaneously at a sampling rate of 200 Hz to ensure capturing detailed arterial pulse waveform morphology. Sensor synchronization was achieved by generating mechanical trigger events (three taps) at the beginning of recording, which produced clear landmarks in all sensors for alignment during post-processing. Participants were instructed to remain still and minimize movements throughout the data collection period to minimize motion artifacts. The experiment setup is illustrated in Fig. 1a.

3.4 Signal Processing

The overall signal processing flow is schematically represented in Fig. 3. The initial signal processing stage involved the acquisition of raw IF signals, characterized by a four-dimensional data structure containing frames, antennas, chirps per frame, and samples per

chirp. Subsequently, a mean removal operation was applied across each chirp to mitigate the presence of DC bias and accentuate the subtle variations indicative of pulsatile activity. Following this, a Fast Fourier Transform (FFT) was performed along the sample dimension for each chirp to extract range-resolved information. From the frequency-domain data, phase were computed using I_{signal} (real) and Q_{signal} (imaginary) components of the signal as [11]:

$$\hat{\phi}(t) = \arctan\left(\frac{I_{\text{signal}}}{Q_{\text{signal}}}\right) \in (-\pi, \pi)\,. \tag{4}$$

To address inherent discontinuities arising from the arctangent function in phase estimation, a temporal phase unwrapping algorithm was implemented. A fourth-order Butterworth bandpass filter (0.5–8 Hz) was applied to attenuate baseline drift and high-frequency noise.

Further processing involved MATLAB peak detection algorithms to the filtered phase signal to identify systolic and diastolic peaks. To optimize signal fidelity, the peak-to-peak value of the pulsating signal was computed across all range bins and antenna elements, and the combination showing the highest peak-to-peak amplitude was selected for further analysis. The identified diastolic peak was strategically utilized to detect potential signal inversions and to ensure the consistent polarity of the arterial pulse wave derived from the mmWave sensor.

For the analysis of the PPG data, one of the green channels of the raw signals was selected. Subsequently, the same bandpass filter that was applied to the mmWave radar data was also implemented on the PPG signal. The remaining steps are peak detection analysis which went through the same pipeline as mmWave signal processing described above to obtain the diastolic peaks. Regarding CNAP data, peak detection was applied to identify the systolic and diastolic peaks to determine blood pressure values. For synchronization of the different sensors, the diastolic peak can serve as a temporal marking point for matching the mmWave, PPG, and CNAP. Also, the IBI were extracted based on the temporal separation between successive diastolic peaks for mmWave and PPG sensors.

The signal morphology was extracted based on the waveform segments between diastolic peaks and normalized, for both amplitude and time domains, for all the sensor systems. This normalization aimed to mitigate the effects of variations in heart rate and signal amplitude, thereby enabling a meaningful comparison of the different sensing modalities.

4 Results

Inter-subject variability in arterial pulse wave morphology obtained by mmWave radar, PPG, and the reference CNAP for a representative subject over a 10-second time period is visually presented in Fig. 4. In particular, the diastolic peaks are marked with dashed lines.

The temporal dynamics of the IBI, derived from the continuous recordings across the entire experimental duration, are illustrated as three distinct time-series in Fig. 5 for Subject1. These signals depict the beat-to-beat variation in the time interval between consecutive diastolic peaks as measured by the mmWave radar, the PPG sensor, and the CNAP gold standard.

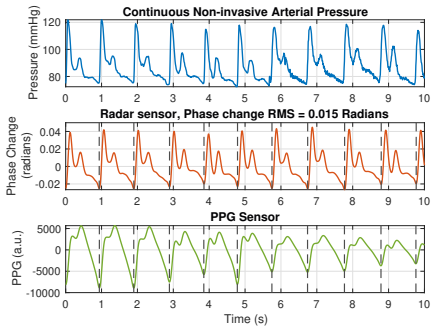

Figure 4: Example simultaneous pulse waveforms over a 10-second period, showing CNAP, radar phase changes, and PPG signals, with detected diastolic peaks indicated by dashed lines.

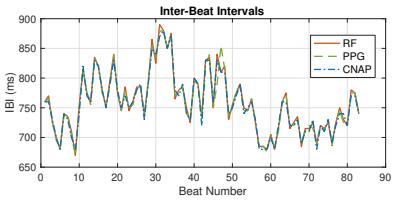

Figure 5: Inter-beat intervals (IBI) of Subject 1, showing the beat-to-beat variation in pulse timing extracted from CNAP, radar, and PPG signals.

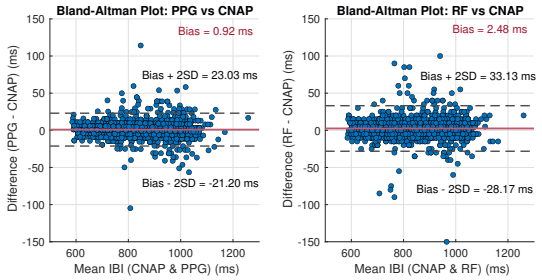

Figure 6: Bland-Altman plot comparing IBI measured by the PPG (left figure), RF (right figure) versus the reference CNAP. The plot shows the differences between the two methods against the mean values. The mean bias and the limits of agreement (±2SD) are shown as reference lines.

To quantitatively assess the agreement between the PPG-derived IBI, mmWave-derived IBI and the CNAP reference IBI, a Bland-Altman analysis was conducted (cf. Fig. 6), which displays the difference between the two IBI measurements plotted against their mean value. The 95% limits of agreement, representing ±2 standard deviations (SD), are indicated by horizontal dashed lines, and the computed bias is represented by a red line.

The IBI, estimated for all test subjects across every heartbeat, yielded a total of 1561 data points measured by both mmWave radar and PPG. These data points can be validated against the CNAP, providing metrics like IBI. The 95% limits of agreement indicate that

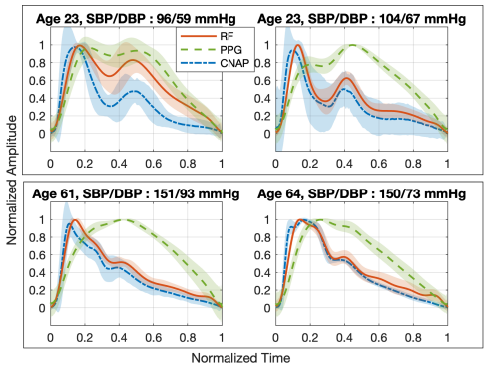

Figure 7: Average normalized pulse waveforms from CNAP, RF, and PPG signals across all detected beats for subjects with different ages. The shaded areas represent ±2 standard deviations, indicating the beat-to-beat variability in pulse morphology for each modality.

Metric	PPG	Reference (CNAP)	Radar
Mean Number of Inflection Points ± STD	1.80 ± 1.09	2.80 ± 1.44	3.11 ± 1.06
Mean Area Under the Curve ± STD	0.61 ± 0.03	0.36 ± 0.05	0.44 ± 0.06
Comparison Metric	**PPG-Ref**	**Radar-Ref**	
Mean Difference in Inflection Points (p-value)	-0.99 (< 0.001)	0.31 (< 0.001)	
Mean Difference in AUC (p-value)	0.25 (< 0.001)	0.08 (< 0.001)	
Mean Cosine Similarity ± STD	0.85 ± 0.04	0.96 ± 0.02	

Table 1: Summary of morphology metrics (top) and statistical comparisons (bottom) for PPG, radar, and reference (CNAP). All metrics were computed separately per subject, and the reported values represent the mean ± standard deviation across subjects, capturing inter-subject variability.

the IBI readings from the PPG sensor can be up to approximately 0.92 ms (bias) - 21.20 ms lower to 0.92 ms (bias) + 23.03 ms higher than expected. Similarly, the IBI readings from the mmWave radar sensor can be up to roughly 2.48 ms (bias) - 28.17 ms lower to 2.48 ms (bias) + 33.13 ms higher than the expected value. The calculated bias value for PPG was 0.92 ms, and for the mmWave radar sensor, it was 2.48 ms. The corresponding RMSE values were 11.09 ms for PPG and 15.52 ms for mmWave radar, further quantifying the average deviation from the reference.

A representation of the average normalized pulse waveform samples for a subset of four participants, selected based on age differences, is shown in Fig. 7. The standard deviations provide a measure of the intra-subject variability of the signals across different cardiac cycles during the experiment, offering insights into the consistency of the pulse waveform within each individual.

The quantitative analysis of arterial pulse waves from different sensor technologies was investigated and demonstrated in Table 1. Inflation points are the number of points where the derivative of

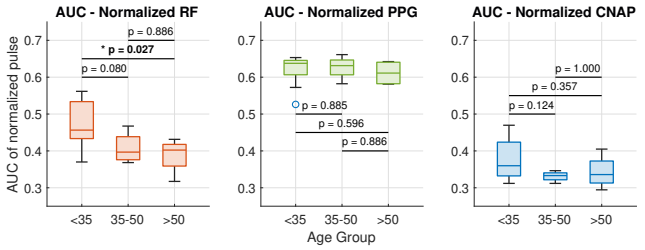

Figure 8: Boxplots of the area under the normalized pulse waveform (AUC) across different age groups for RF, PPG, and CNAP modalities.

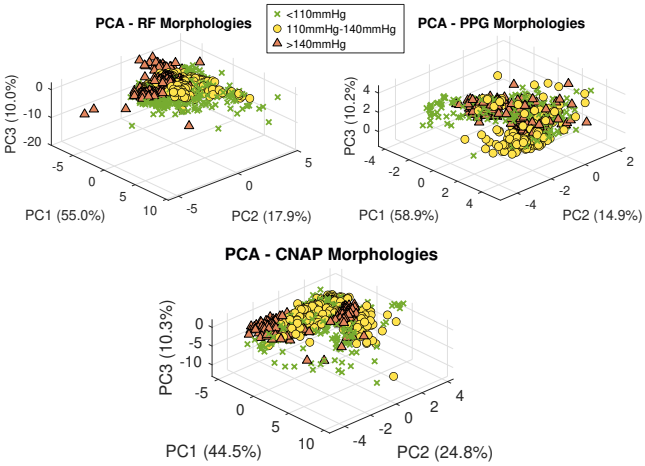

Figure 9: Principle component analysis of different sensing modalities, marked by different systolic blood pressure ranges.

the signal is equal to zero and averaged through the experiment and the area under curve (AUC) is the integration of the wave. In addition, the table reports the difference between the metrics estimated by different technologies versus gold standard.

The AUCs of different sensor modalities for different age groups are demonstrated in Fig. 8. The AUC of arterial pulse waveform shows lower range for RF and CNAP comparing with PPG. Additionally, the statistical significance (p-values) of the differences between age groups is highlighted, with the RF modality demonstrating the lowest p-value, indicating the strongest distinction between young and older participants.

The statistical analysis of different sensor modalities categorized by systolic blood pressure ranges: below 110 mmHg, 110-140 mmHg, and above 140 mmHg is demonstrated in Fig. 9. The first three principle components show the main variation in morphologies.

5 Discussion

The mmWave sensor tracks pulse wave morphology with noticeable similarity to CNAP. The phase variation of the radar presents a stable signal throughout the heartbeats, and as visible in Fig. 4. Upon inspecting the arterial waveforms, it is noticeable that reflections occur after the systolic peak, appearing as some peaks in the

waveform and dicrotic notch which can be a signature in the waveform originating from the mechanical properties of the arteries. The mmWave sensor captures these reflections in amplitude and time. PPG occasionally misses reflections due to blood transition to capillaries and slower pulse decay, reducing their visibility.

The Bland-Altman IBI plots indicate an acceptable level of agreement between PPG with the reference. It shows the potential of PPG sensor for continuous IBI measurement.

The mmWave sensor demonstrates a significant capability in capturing the details of the arterial pulse wave, including the Late Systolic Augmentation Wave and the reflection waves. This highlights a crucial benefit of cuff-less mmWave sensing: the ability for continuous monitoring of the arterial pulse wave, which is a vital step towards applications such as improved sleep monitoring and the continuous assessment of cardiovascular health. The high sensitivity of mmWave radar to arterial pulsations positions it as a promising tool for in-depth cardiovascular assessment.

The comparison of normalized arterial pulse waveforms obtained from three sensing modalities in Fig. 7 illustrates four distinct examples of pulse wave morphologies. The temporal alignment between the CNAP and mmWave waveforms is notably higher when contrasted with the PPG waveform. The PPG waveform typically presents as broader with a more gradual decay, whereas CNAP and mmWave exhibit sharper signals with more defined upslopes, more closely resembling the expected characteristics of arterial waveform. Both the CNAP and mmWave signals effectively detect the dicrotic notch. In contrast, the PPG signal often exhibits a smoother decay due to its nature as a blood volume–based sensor. The variability in the signals shows the consistency and repeatability of the sensor technology. When compared to PPG, the mmWave radar demonstrates a very similar pulse wave morphology to CNAP, and the confidence intervals associated with the mmWave data suggest stability.

Fig.7 shows age-related differences in arterial pulse morphology across four representative participants. Younger subjects show late reflections (0.5s), while older ones exhibit dicrotic notch loss and broader systolic peaks. These changes are consistent with prior studies[7, 15, 23, 28], reflecting the known effect of age-related arterial stiffness on waveforms.

The quantitative analysis in Table 1 shows that the mean number of inflection points in PPG, CNAP, and radar are 1.8, 2.8, and 3.1, respectively, which shows that the mmWave sensor is capable of detecting the reflected waves similar to the reference device. The mean AUC, demonstrated that the reflective PPG has a higher value, indicating the slow decaying of the PPG signal. The mean AUC of reference and CNAP are 0.36 and 0.44, show the similarity between these two waveforms. According to the statistical comparison in Table 1, the reflective PPG is missing one inflection point on average compared to the reference, and the mmWave-based sensor can detect the inflection points which was detected by the reference device. The mean AUC comparison demonstrates a 0.25 higher value compared to the reference which emphasize on the slow decay of PPG, while the difference between mmWave and reference is 0.08, which shows an acceptable level of agreement for AUC. Finally, the cosine similarity for reference against PPG and mmWave is 0.85 and 0.96, shows that the mmWave-based signal is more aligned with the reference waveform.

The AUC of normalized pulse wave in Fig. 8 shows a decreasing trend with age for RF sensor modality. By ageing the reflected peak shift closer to the systolic peak and it increases the amplitude of systolic peak, but due to the normalization, this effect can not be visible. Since the arterial pulse waveforms are normalized both in amplitude and time, the more pronounced secondary peak in younger group leads to more AUC values.

The PCA distributions reveal that the RF sensor morphology clusters are distinctly separated by blood pressure groups. The variation in morphology is mostly caused by variation among different test participants. This shows the potential of RF sensor for blood pressure and arterial stiffness estimation.

PPG operates by detecting changes in blood volume, while the mmWave radar is sensitive to the mechanical deformation of tissues resulting from arterial pulsation. This fundamental difference suggests that by combining the information obtained from both PPG and mmWave sensors, it may be possible to gain a more comprehensive understanding of cardiovascular mechanics.

6 Conclusion

The study demonstrated the potential of the wearable device hosting a mmWave sensor to capture the arterial pulse wave with a morphology similar to that obtained from the cuff-based reference. In addition PPG demonstrated sufficient accuracy in tracking IBI, enabling it's use in continuous stress level monitoring. Among the modalities, RF demonstrated the largest AUC shift with age, indicating its potential for vascular ageing assessment.

Our results highlight that integrating both sensors into one wearable system allows the device to benefit from continuous, low-power IBI tracking via PPG, while mmWave radar enables high-fidelity arterial pulse waveform acquisition at selected intervals—something not feasible using green PPG alone. This complementary behavior strengthens the device's overall capacity for cardiovascular health assessment.

Limitations and Future Work

The current study's conclusion is based on 23 test participants, it is recommended that there be more variation in the test participants and a better balance between categories like gender and health conditions. The PPG signal was derived from the green channel, which offers limited morphological accuracy; a multi-wavelength approach could provide a more comprehensive evaluation. In addition, a more in-depth analysis of the mmWave-based waveform morphology is to be conducted using advanced feature extraction. Future research will establish a connection between the details present in the mmWave signal and the mechanical properties of the arteries, such as arterial stiffness. The system's performance under real-world, dynamic conditions will also be evaluated, and future applications such as non-invasive blood pressure estimation will be explored.

Acknowledgments

We acknowledge partial funding by the Finnish Doctoral Program Network in Artificial Intelligence, AI-DOC (decision number VN/3137/2024-OKM-6). The authors gratefully acknowledge ams-osram for generously providing the optical biosensing development kit.

References

[1] Serene Abu-Sardanah, Ali Gharamohammadi, Omar M. Ramahi, and George Shaker. 2023. A Wearable mm-Wave Radar Platform for Cardiorespiratory Monitoring. *IEEE Sensors Letters* 7, 6 (2023), 1–4. doi:10.1109/LSENS.2023.3277365

[2] John Allen. 2007. Photoplethysmography and its application in clinical physiological measurement. *Physiological measurement* 28, 3 (2007), R1.

[3] AMS Osram. 2025. AMS AS7058 EVM-EB Evaluation Kit. https://ams-osram.com/products/boards-kits-accessories/kits/ams-as7058-evm-eb-evaluation-kit. Accessed: 2025-05-21.

[4] AMS Osram. 2025. AMS AS7058 EVM-EB Extension Evaluation Kit. https://ams-osram.com/products/boards-kits-accessories/kits/ams-as7058-evm-eb-extension-evaluation-kit. Accessed: 2025-05-21.

[5] AMS Osram. 2025. AMS AS7058 High-Performance Vital Sign Analog Frontend. https://ams-osram.com/products/sensor-solutions/analog-frontend/ams-as7058-high-performance-vital-sign-analog-frontend. Accessed: 2025-05-21.

[6] Asiful Arefeen, Ali Akbari, Seyed Iman Mirzadeh, Roozbeh Jafari, Behrooz A. Shirazi, and Hassan Ghasemzadeh. 2024. Inter-Beat Interval Estimation with Tiramisu Model: A Novel Approach with Reduced Error. *ACM Trans. Comput. Healthcare* 5, 1, Article 1 (Jan. 2024), 19 pages. doi:10.1145/3616020

[7] Alberto Avolio, Mark Butlin, and Andrew Walsh. 2010. Arterial blood pressure measurement and pulse wave analysis—Their role in enhancing cardiovascular assessment. *Physiological measurement* 31 (01 2010), R1–47. doi:10.1088/0967-3334/31/1/R01

[8] Graham M Brooker et al. 2005. Understanding millimetre wave FMCW radars. In *1st international Conference on Sensing Technology*, Vol. 1.

[9] C. H. Chen, T. H. Tao, Y. H. Chou, Y. W. Chuang, and T. B. Chen. 2021. Arteriovenous Fistula Flow Dysfunction Surveillance: Early Detection Using Pulse Radar Sensor and Machine Learning Classification. *Biosensors (Basel)* 11, 9 (2021). doi:10.3390/bios11090297 2079-6374 Chen, Cheng-Hsu Orcid: 0000-0002-1299-5055 Tao, Teh-Ho Chou, Yi-Hua Chuang, Ya-Wen Chen, Tai-Been Orcid: 0000-0002-3348-4422 TCVGH-VHCY1098602/Taichung Veterans General Hospital and Taichung Veterans General Hospital, Chiayi Branch/ Journal Article Switzerland 2021/09/26 Biosensors (Basel). 2021 Aug 26;11(9):297. doi: 10.3390/bios11090297..

[10] Philip Jan Claessens, Ruth Peeters, Louis Claessens, Christophe Claessens, Jan Claessens, and Philip Maria Claessens. 2023. Pulse wave analysis measurements: important, underestimated and undervalued parameters in cardiovascular health problems. *Frontiers in Cardiovascular Medicine* 10 (2023), 1266258.

[11] Shatabdi Das, Girish Dwivedi, Hadi Afsharan, and Omid Kavehei. 2024. A Non-Invasive and Non-Contact Jugular Venous Pulse Measurement: A Feasibility Study. *medRxiv* (2024), 2024.06.04.24308313. doi:10.1101/2024.06.04.24308313

[12] Felipe M Dias, Diego AC Cardenas, Marcelo AF Toledo, Filipe AC Oliveira, Estela Ribeiro, Jose E Krieger, and Marco A Gutierrez. 2025. Exploring the limitations of blood pressure estimation using the photoplethysmography signal. *Physiological Measurement* 46, 4 (2025), 045007.

[13] E. Gomes, R. Naima, C. Liao, and O. Shay. 2022. Waveform Morphology Comparison in Wearable Blood Pressure Sensors. In *2022 44th Annual International Conference of the IEEE Engineering in Medicine & Biology Society (EMBC)*. 2902–2905. doi:10.1109/EMBC48229.2022.9870890

[14] Unsoo Ha, Salah Assana, and Fadel Adib. 2020. Contactless seismocardiography via deep learning radars. In *Proceedings of the 26th annual international conference on mobile computing and networking*. 1–14.

[15] Martti Ilvesmäki, Hany Ferdinando, Kai Noponen, Tapio Seppänen, Vesa Korhonen, Vesa Kiviniemi, and Teemu Myllylä. 2025. Age group classification based on optical measurement of brain pulsation using machine learning. *Scientific Reports* 15, 1 (2025), 3166.

[16] Infineon Technologies AG. 2025. BGT60TR13C - 60 GHz Radar Sensor. https://www.infineon.com/cms/en/product/sensor/radar-sensors/radar-sensors-for-iot/60ghz-radar/bgt60tr13c/. Accessed: 2025-05-21.

[17] Infineon Technologies AG. 2025. DEMO BGT60TR13C. https://www.infineon.com/cms/en/product/evaluation-boards/demo-bgt60tr13c/. Accessed: 2025-05-21.

[18] J. Johnson, C. Kim, and O. Shay. 2019. Arterial Pulse Measurement with Wearable Millimeter Wave Device. In *2019 IEEE 16th International Conference on Wearable and Implantable Body Sensor Networks (BSN)*. 1–4. doi:10.1109/BSN.2019.8771037

[19] J. E. Johnson, O. Shay, C. Kim, and C. Liao. 2019. Wearable Millimeter-Wave Device for Contactless Measurement of Arterial Pulses. *IEEE Trans Biomed Circuits Syst* 13, 6 (2019), 1525–1534. doi:10.1109/tbcas.2019.2948581 1940-9990 Johnson, Jessi E Shay, Oliver Kim, Chris Liao, Catherine Journal Article Research Support, Non-U.S. Gov't Research Support, U.S. Gov't, Non-P.H.S. United States 2019/10/22 IEEE Trans Biomed Circuits Syst. 2019 Dec;13(6):1525-1534. doi: 10.1109/TBCAS.2019.2948581. Epub 2019 Oct 21..

[20] C. Li, S. Zheng, X. Hui, and X. Zhang. 2024. Electromagnetic Effective Coupling and High Spatial Resolution Theory in Near-Field Cardiac Sensing. *IEEE Transactions on Microwave Theory and Techniques* 72, 4 (2024), 2283–2297. doi:10.1109/TMTT.2023.3346680

[21] C. Liao, O. Shay, E. Gomes, and N. Bikhchandani. 2021. Noninvasive Continuous Blood Pressure Measurement with Wearable Millimeter Wave Device. In *2021 IEEE 17th International Conference on Wearable and Implantable Body Sensor Networks (BSN)*. 1–5. doi:10.1109/BSN51625.2021.9507020

[22] Suril Mehta, Nipun Kwatra, Mohit Jain, and Daniel McDuff. 2024. Examining the challenges of blood pressure estimation via photoplethysmogram. *Scientific Reports* 14, 1 (2024), 18318.

[23] Wilmer W Nichols. 2005. Clinical measurement of arterial stiffness obtained from noninvasive pressure waveforms. *American journal of hypertension* 18, S1 (2005), 3S–10S.

[24] Wilmer W Nichols, Scott J Denardo, Ian B Wilkinson, Carmel M McEniery, John Cockcroft, and Michael F O'Rourke. 2008. Effects of arterial stiffness, pulse wave velocity, and wave reflections on the central aortic pressure waveform. *The journal of clinical hypertension* 10, 4 (2008), 295–303.

[25] Amashi Niwarthana, Pamuditha Somarathne, Pierre Qian, Ken-Tye Yong, and Anusha Withana. 2024. Efficient and Robust Heart Rate Estimation Approach for Noisy Wearable PPG Sensors Using Ideal Representation Learning. In *Proceedings of the 2024 ACM International Symposium on Wearable Computers* (Melbourne VIC, Australia) *(ISWC '24)*. Association for Computing Machinery, New York, NY, USA, 1–8. doi:10.1145/3675095.3676606

[26] Malikeh Pour Ebrahim, Fatemeh Heydari, Taiyang Wu, Katherine Walker, Keith Joe, Jean-Michel Redoute, and Mehmet Rasit Yuce. 2019. Blood pressure estimation using on-body continuous wave radar and photoplethysmogram in various posture and exercise conditions. *Scientific Reports* 9, 1 (2019), 16346.

[27] M. M. Y. R. Riad and G. Shaker. 2024. Radar-Based Human Pulse Sensing through a Resonator-Based Superstrate. In *2024 IEEE MTT-S International Microwave Biomedical Conference (IMBioC)*. 18–20. doi:10.1109/IMBioC60287.2024.10590432

[28] Satoru Sakuragi and Walter P Abhayaratna. 2010. Arterial stiffness: methods of measurement, physiologic determinants and prediction of cardiovascular outcomes. *International journal of cardiology* 138, 2 (2010), 112–118.

[29] Francesco Scardulla, Gloria Cosoli, Susanna Spinsante, Angelica Poli, Grazia Iadarola, Riccardo Pernice, Alessandro Busacca, Salvatore Pasta, Lorenzo Scalise, and Leonardo D'Acquisto. 2023. Photoplethysmograhic sensors, potential and limitations: Is it time for regulation? A comprehensive review. *Measurement* 218 (2023), 113150.

[30] Zhenguo Shi, Tao Gu, Yu Zhang, and Xi Zhang. 2023. mmBP: Contact-Free Millimetre-Wave Radar Based Approach to Blood Pressure Measurement. 667–681 pages. doi:10.1145/3560905.3568506

[31] C. H. Tseng, T. J. Tseng, and C. Z. Wu. 2020. Cuffless Blood Pressure Measurement Using a Microwave Near-Field Self-Injection-Locked Wrist Pulse Sensor. *IEEE Transactions on Microwave Theory and Techniques* 68, 11 (2020), 4865–4874. doi:10.1109/TMTT.2020.3011446

[32] Tzu-Jung Tseng and Chao-Hsiung Tseng. 2020. Noncontact wrist pulse waveform detection using 24-GHz continuous-wave radar sensor for blood pressure estimation. In *2020 IEEE/MTT-S International Microwave Symposium (IMS)*. IEEE, 647–650.

[33] N. Vysotskaya, N. Maul, A. Fusco, S. Hazra, J. Harnisch, T. Arias-Vergara, and A. Maier. 2024. Transforming Cardiovascular Health: a Transformer-Based Approach to Continuous, Non-Invasive Blood Pressure Estimation via Radar Sensing. In *ICASSP 2024 - 2024 IEEE International Conference on Acoustics, Speech and Signal Processing (ICASSP)*. 2041–2045. doi:10.1109/ICASSP48485.2024.10446988

[34] Fengyu Wang, Xiaolu Zeng, Chenshu Wu, Beibei Wang, and K.J. Ray Liu. 2021. mmHRV: Contactless Heart Rate Variability Monitoring Using Millimeter-Wave Radio. *IEEE Internet of Things Journal* 8, 22 (2021), 16623–16636. doi:10.1109/JIOT.2021.3075167

[35] Guochao Wang, José-María Muñoz-Ferreras, Changzhan Gu, Changzhi Li, and Roberto Gómez-García. 2014. Application of Linear-Frequency-Modulated Continuous-Wave (LFMCW) Radars for Tracking of Vital Signs. *IEEE Transactions on Microwave Theory and Techniques* 62, 6 (2014), 1387–1399. doi:10.1109/TMTT.2014.2320464

[36] L. Wen, S. Dong, Z. Zhang, C. Gu, and J. Mao. [n. d.]. Noninvasive Continuous Blood Pressure Monitoring Based on Wearable Radar Sensor with Preliminary Clinical Validation. In *2022 IEEE/MTT-S International Microwave Symposium - IMS 2022*. 707–710. doi:10.1109/IMS37962.2022.9865440

[37] L. Wen, S. Q. Dong, C. Z. Gu, and J. F. Mao. 2022. Antenna-in-Package Millimeter-Wave Sensor for Monitoring Heart Rate Variability. *2022 Ieee 10th Asia-Pacific Conference on Antennas and Propagation, Apcap* (2022). doi:10.1109/Apcap56600.2022.10069609 Bv1ax Times Cited:0 Cited References Count:7 Asia Pacific Conference on Antennas and Propagation.

[38] Zixin Zheng, Yumeng Liang, Rui Lyu, Junjie Bao, Yiwen Huang, Anfu Zhou, Huadong Ma, Jingjia Wang, Xiangbin Meng, Chunli Shao, Yida Tang, and Qian Zhang. 2024. BP3: Improving Cuff-less Blood Pressure Monitoring Performance by Fusing mmWave Pulse Wave Sensing and Physiological Factors: BP3: Cuffless BP Monitoring by Fusing mmWave Pulse Wave Sensing and Physiological Factors. 730–743 pages. doi:10.1145/3666025.3699370